

LASER INTERFEROMETER GRAVITATIONAL WAVE OBSERVATORY
- LIGO -
CALIFORNIA INSTITUTE OF TECHNOLOGY
MASSACHUSETTS INSTITUTE OF TECHNOLOGY

Presentation	LIGO-G2401688-v2	09/15/2024
Mapping and Correcting the Wavefront of the GQuEST End Mirrors		
Erin McGee Mentor: Daniel Grass Faculty Mentor: Prof. Lee McCuller		

California Institute of Technology
LIGO Project, MS 18-34
Pasadena, CA 91125
Phone (626) 395-2129
Fax (626) 304-9834
E-mail: info@ligo.caltech.edu

Massachusetts Institute of Technology
LIGO Project, Room NW17-161
Cambridge, MA 02139
Phone (617) 253-4824
Fax (617) 253-7014
E-mail: info@ligo.mit.edu

LIGO Hanford Observatory
Route 10, Mile Marker 2
Richland, WA 99352
Phone (509) 372-8106
Fax (509) 372-8137
E-mail: info@ligo.caltech.edu

LIGO Livingston Observatory
19100 LIGO Lane
Livingston, LA 70754
Phone (225) 686-3100
Fax (225) 686-7189
E-mail: info@ligo.caltech.edu

Abstract

GQuEST, or Gravity from the Quantum Entanglement of Space-Time, is an experiment with the goal of measuring fluctuations in space time using an ultra-sensitive tabletop Michelson Interferometer. This experiment requires high precision optics, including extremely thin high-reflectivity mirrors. This makes the optics extremely sensitive to small changes in their radius of curvature which can cause a misalignment in the modes of the light in the system. This can, in part, be mitigated by imaging the mirrors and matching the modes and by applying pressure to the mirror in a custom mount. The goal of this project is to develop a process for imaging and correcting the curvature of the mirror and analyzing how well the modes of different mirrors match.

1 Introduction

Einstein's theory of general relativity and quantum mechanics both make accurate and well-tested predictions. However, these theories are generally incompatible. The aim of studying 'quantum gravity' is to propose descriptions of gravity that are in keeping with our understanding of quantum mechanics. While there have been many proposed theories centered around what the quantum nature of gravity is, such theories are extremely hard to verify experimentally, due to the scales at which phenomena must be measured. One such theory of quantum gravity, proposed by Erik Verlinde and Kathryn Zurek, argues that the holographic principle provides us with a way to quantize spacetime [1]. These fluctuations, referred to now as VZ fluctuations, could potentially be observed using precise optical techniques, and measuring the Power Spectral Density (PSD) of these proposed fluctuations which are in concept observable using tabletop optics. These fluctuations are extremely weak in amplitude, although they are in principle measurable in a realistic experiment. This is one of the reasons this effect has not been measured, as low amplitudes are harder to detect because they are below quantum noise. These fluctuations are also stochastic in nature, and therefore must be described statistically, which is why quantum gravity experiments such as this use a PSD measurement to observe phase difference by measuring photons at different frequencies [2].

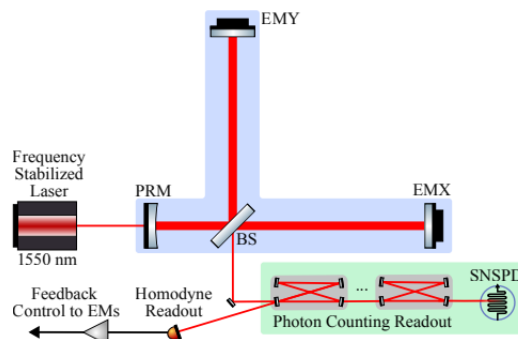


Figure 1: Michelson Interferometer in GQuEST setup

GQuEST, or Gravity from the Quantum Entanglement of Space-Time, is an project that is designed to measure this phase difference by using a Michelson interferometer like LIGO, as can be seen in Fig. 1. The interferometer splits light from a laser into two separate arms at the beamsplitter, where they are then reflected by end mirrors and recombine. The light then moves into the photon counting readout scheme, which is a method that measures light output by counting single photons rather than using the typical homodyne readout. This method has yet to be applied to interferometer measurements, and provides some new advantages to the setup, namely that the interferometer is far more sensitive than it would be with the homodyne readout.

This will be a key improvement of GQuEST from similar interferometer experiments used to study quantum gravity. It would provide some new advantages to the setup, namely that the interferometer is far more sensitive than it would be with homodyne readout [2]. GQuEST would not be limited by quantum noise because of the photon counting method, it is instead limited by classical noise, which is much lower in amplitude.

2 Motivation

2.1 Radius of Curvature

For this project, I focused on the end mirrors of the GQuEST Interferometer, which has two, highly reflective, silicon mirrors. Standard, thicker mirrors would be a dominant source of classical noise in the interferometer, caused in part to the vibrational modes of the mirrors. This noise can be reduced to be below coating thermal noise by making the mirrors extremely thin, around 2 mm. The mirrors have a highly reflective (HR) Bragg reflection coating applied to the surface which applies a stress to the mirror itself. This in turn increases wavefront curvature, which is reflected in the radius of the curvature of the mirror itself and can be described as:

$$r_{curv} \approx \frac{1}{6} \left(\frac{E_s h^2}{\sigma_c h_c (1 - \nu_s)} \right) \quad (1)$$

where E_s is Young's modulus of the applied substrate, or the stiffness of the mirror, h is the thickness of the end mirror, σ_c is the coating stress, h_c is the thickness of the coating, and ν_s is the Poisson ratio for silicon [2]. As the wavefront curvature increases so does the amount of light that leaks out of the interferometer, called contrast defects. This is because differences in curvature between the two mirrors can lens the light into different spatial modes that do not fully cancel when the light interferes at the beamsplitter, resulting in an excess of light in our readout. This effect can be mitigated in part by applying a thick anti-reflective coating to the back of the mirror, which will partially reduce the curvature caused by the thickness of the HR coating. Reducing contrast defects can also be done by adjusting the curvature difference between the two mirrors. This difference can be found by subtracting the curvature, in diopters, of each of the end mirrors. The goal is such that the mirrors have the same curvature and therefore produce the same optical mode and have the same expected amplitude coefficients.

We can determine the optical modes of light coming from a mirror by calculating the coupling coefficient of the light. This tells us 'how much' of the incoming beam is contained in our outgoing beam. This coefficient is given by solving the overlap integral of the amplitude of the incoming and outgoing beams. This can be done by the following:

$$k_{nmn'm'}(x, y) = \int \int u_{n'm'}^*(x, y) e^{ik\phi(x, y)} u_{nm}(x, y) dx dy \quad (2)$$

where k is the wave number, ϕ is the phase information from the wavefront of the beam, and u is a function for the beam given by:

$$u_{nm}(x, y) = \left(\frac{1}{2^{n+m-1} n! m! \pi} \right)^{1/2} \left(\frac{1}{w_0} \right) \left(\frac{q_0}{q(z)} \right) \left(\frac{q_0 q^*(z)}{q_0^* q(z)} \right)^{n+m/2} H_n \left(\frac{\sqrt{2}x}{w(z)} \right) H_m \left(\frac{\sqrt{2}y}{w(z)} \right) \exp \left(-ik \frac{(x^2 + y^2)}{2q(z)} \right) \quad (3)$$

where n and m are integers, w_0 is the beam waist, $w(z)$ is the beam width, q is the complex beam parameter, k is the wave number, x and y are the transverse directions of the wave, z as the beam axis, and H a Hermite Polynomial of order n or m [3]. HG_{mn} is our notation for referring to a beam with m and n modes.

By determining the coupling coefficient of the light reflected off of our mirror, which can be done using wavefront measurement methods discussed in Section 3, we can solve for the radius of curvature of the mirror. The derivation for this is expanded on in Section 6, and provides us with the result:

$$D_{00} = \frac{-4i}{kw^2} \left(1 - \frac{1}{k_{00}^2} \right) \quad (4)$$

$$D_{02} \approx \frac{4\sqrt{2}k_{02}}{kw^2} \quad (5)$$

Since we can calculate a different coupling coefficient for each of the different modes, we can also calculate a different radius of curvature for each of the different modes, hence why there are multiple equations for curvature. The array of these radius values fully describe the curvature over different mode configurations.

How much control we have over the mirror in terms of how much we can change the radius can give us an indication of how well we can match two mirrors in the final GQuEST setup, or if any changes need to be made. This can provide us with a baseline to test our methods by since the uncoated mirror can be assumed to be flat. The goal of this project is to see how much we can change the radius of curvature of the mirror in order to counteract the eventual curvature of the coated mirrors.

2.2 End Mirror Mount

While there are many different forms of 'adaptive optics', for this project, we still need to maintain a high quality factor of the mirror and be precise in our ability to change the radius as we can reasonably be. This led to the current design for the end mirror mount, shown in Fig. 2, that was designed by my mentor Daniel Grass. The design has two metal "half rings" that hold the silicon mirror in place. Each half ring has two spokes, that are held in place by a small strip of indium foil. They are clasped by a T shaped holder that we call a 'T', which are movable clamps that can be seen in Fig. 3. When pressure is applied to these 'T's by a set of adjustable screws, the spokes of the mirror are moved, which in turn deforms the mirror and changes the radius of curvature. This then changes the coupling coefficient of the light, which we can observe in the wavefront.

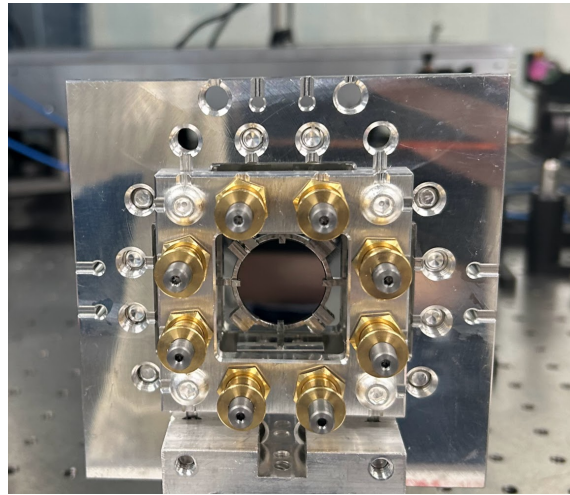


Figure 2: End Mirror Mount (back view)

We want to have a great deal of control over exactly how we are curving the mirror. This we can do by accounting for the mode that the wavefront is in. This is done through a special function know as Zernike polynomials, which are orthogonal on the unit disk [4] and described in Section 6.

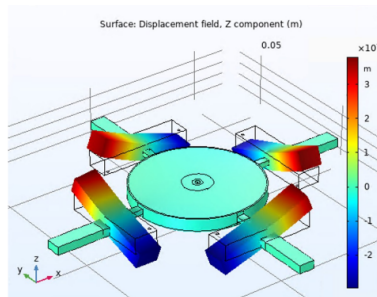


Figure 3: End Mirror Mount in COMSOL

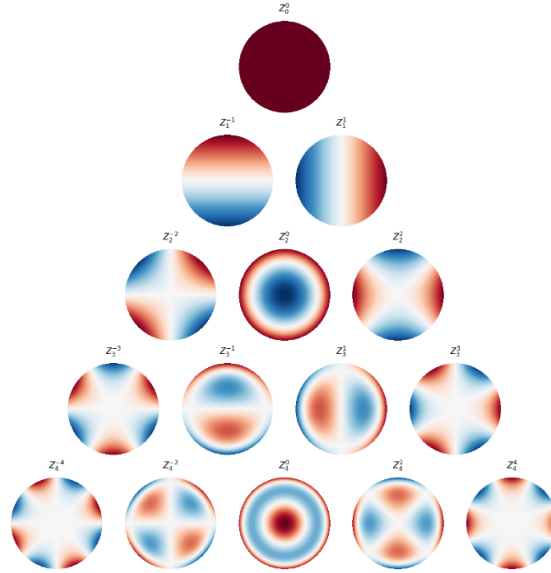


Figure 4: First 15 Zernike Polynomials

These deformations are helpful to describing how the mirror is being curved. The first three modes, the piston, y-tilt, and x-tilt, can be changed simply by moving the position of the mirror and its mount. The next three modes actually require us to change the surface of the mirror. The astigmatic modes are when $j = 3$ and when $j = 5$, and can be identified by the characteristic cross shapes in Fig. 4. The defocus mode, which takes place when $j = 4$ has a kind of circle shape on the disk. All of these shapes can be physically made with the mirror by applying a certain force with the adjustment screws. Our goal is to see a wavefront that is similar in appearance to $j = 3$, $j = 4$, and $j = 5$. When the mirror is coated, and the mirror is curved by this coating, then we can use this control we have over the mirrors to cancel out the curvature, and have a flat mirror that can be mode matched to the corresponding mirror in the interferometer in the GQuEST setup.

3 Methods

I used two main methods in order to measure the wavefront of the light reflected off of the mirror. The goal with these measurements is to obtain an accurate phase map of the wavefront, so that we can use Eq. (2) to solve for the coupling coefficient of the light incident on and reflected out of the mirror. This then allows us to solve for the radius of curvature of the mirror. These wavefront measurement methods are Fizeau interferometers and Shack-Hartmann Wavefront Sensors.

Fizeau interferometers are able to analyze the interference fringes from the wavefront of the mirror. Since the spatial separation and intensity of the fringes is related to the shape of the mirror, we can use this to determine what the surface looks like. For example, a perfectly

flat mirror would show even spaced straight line fringes, so any curvature or roughness of the mirror's surface changes the location and intensity of the predicted fringes. Since the incident angle, intensity, slope angle, wavelength, distance, and most other parameters of the device are known, we can reconstruct the surface of the mirror using these fringe patterns [5]. This can be seen in Fig. 5, and this Fizeau interferometer was used to measure the wavefronts of the LIGO Test Masses as well.

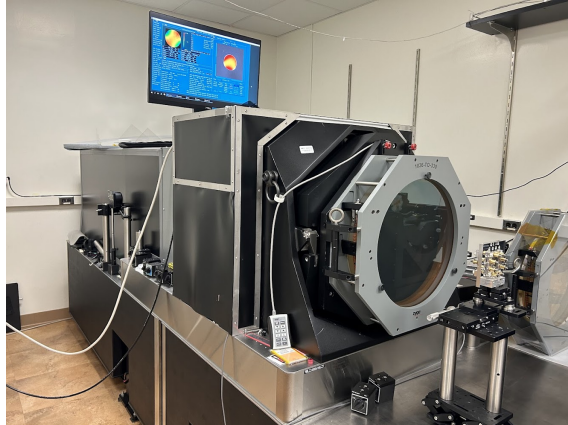


Figure 5: Fizeau interferometer

Shack-Hartman wavefront sensors are used to measure the shape of a wavefront from incident light. It consists of an array of microlenses, as can be seen in Fig. 6, usually made of fused silica, which can be either mounted or unmounted [6]. This array is in front of an image sensor, which allows us to estimate the wavefront distortions from the light.

Each of the small lenses produces an intensity profile. This intensity is related to the spatial Fourier transform (since each of the smaller lenses in the array has a discrete intensity). This intensity is shifted by distortions in the wavefront, so while a planar wavefront will have one point of intensity at the center of each microlens, a distorted wavefront will shift each of them, so the wavefront can be reconstructed by analyzing this shift. One disadvantage is that the resolution is limited by how many microlenses there are and how far apart they are. The model we are using from Thorlabs has 30 by 30 smaller lenses in this array.

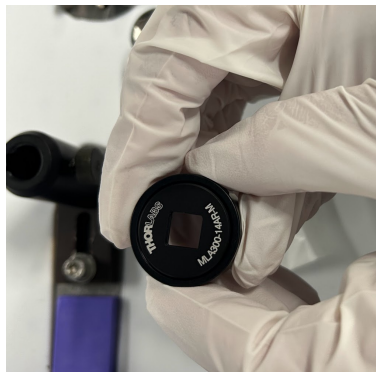


Figure 6: Microlens array

The wavefront is reconstructed also using Zernike Polynomials, discussed earlier, since the coefficients of the wavefront can be found which by fitting the local slope of the wavefront error with Zernike polynomial derivatives. The shift in the lens' image is proportional to the mean slope of the wavefront on the lens, which approximates the slope of the wavefront. This process is elaborated on in Section 6.

The first step I took in this project was to use the Fizeau interferometer to image the uncoated silicon mirror without it being in the mirror mount. This would provide us with a baseline of what the unstressed mirror looked like, and allow us to refine our process of analyzing the data from the Fizeau interferometer.

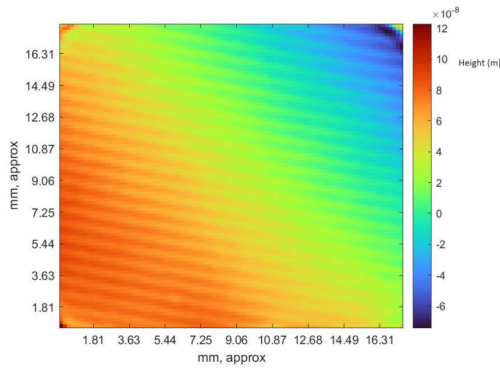


Figure 7: Wavefront image of the uncoated mirror

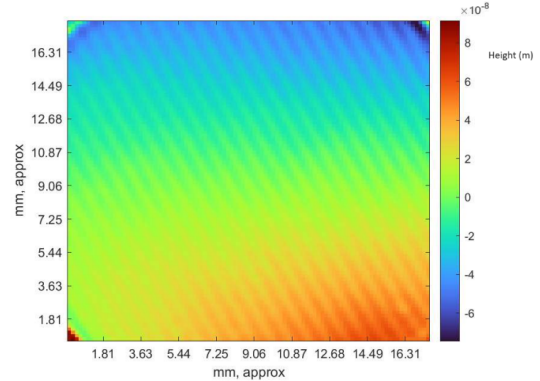


Figure 8: Wavefront image of the uncoated mirror rotated 45 degrees

From this wavefront data, I was able to develop a process in python that used the data from the Fizeau interferometer to calculate the coupling coefficient of the beam from the HG_{00} mode to the HG_{mn} mode, where m and n describe the outgoing beam. From this, I can then calculate the radius of curvature of the mirror. I also used this to simulate what the expected radius of curvature would be for some applied force on the mirror. This was done using COMSOL, a finite element analysis software. Using the design of the end mirror mount in this program, I could adjust the simulated force applied on the mirror. I could then use this simulation to find what the expected coupling coefficients would be for a mirror of that radius. This gave us an indication of what to expect when I adjusted the mirror itself.

Using the Shack-Hartmann Wavefront Sensor required us to research and purchase the microlens array as seen in Fig. 6, and then to design and build a setup for using the array.

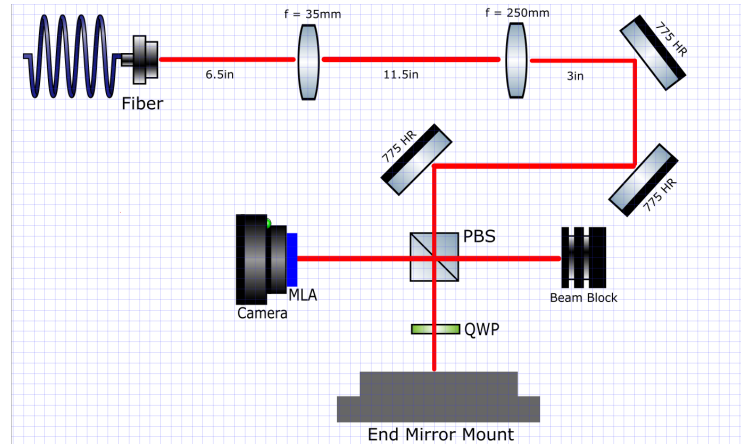


Figure 9: Setup for the Shack-Hartman Interferometer

In the design in Fig. 9, we collimate the light out of the fiber optic cable by passing it through two lenses. Light would then pass through a polarizing beamsplitter, then to a quarter waveplate, giving it a circular polarization of 45 degrees from the plates axis. Then it would reflect off of the mirror we are testing, pass through the quarter waveplate again for a total polarization shift of 90 degrees from the axis and then through the beamsplitter again. Then the light will pass into the mounted lens array (MLA) and then to the camera. The wavefront sensor is an MLA with a square grid of smaller lenses that measure the intensity, which is how the wavefront is reconstructed.

We used this setup to image the flat mirror, in order to compare it to the data we had already taken with the Fizeau interferometer. After that, we used the same process as before to evaluate the coupling coefficient and the radius of curvature of the wavefront. Finally, we imaged the same modes with the Fizeau interferometer again to compare our results.

4 Results

4.1 Simulation results

Using an expected radius we obtained from COMSOL, we are able to calculate the Zernike coefficients for what an expected wavefront of a certain mode. Using this data, we can calculate what the expected coupling coefficient for a certain mode and radius would be. This is expanded on in Section 6.

From this simulation, we can find which mode the wavefront is most coupled to. This gives us a rough idea of how to judge how effective our actual mirror is coupling to a certain mode.

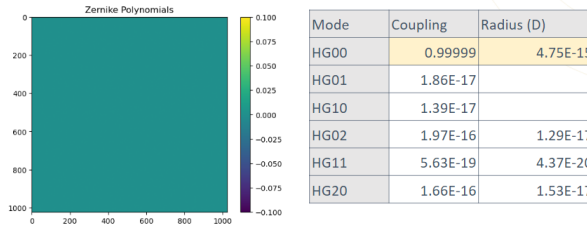


Figure 10: Flat Mirror Simulation

We also evaluated the oblique astigmatic mode (plus shape) shown below.

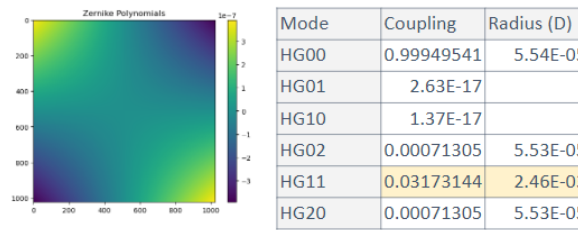


Figure 11: Oblique Astigmatic Mode Simulation

This mirror shape couples most strongly to the HG_{11} mode. This means we can expect a similar result with our actual mirror.

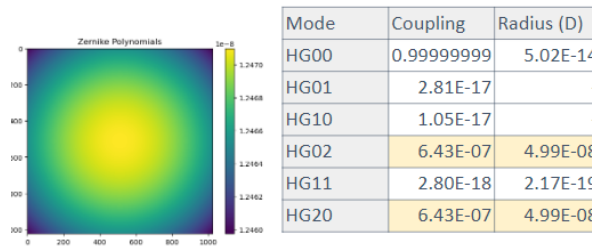


Figure 12: Defocus Mode Simulation

The defocus mode shown above most strongly couples to the HG_{20} and HG_{02} modes.

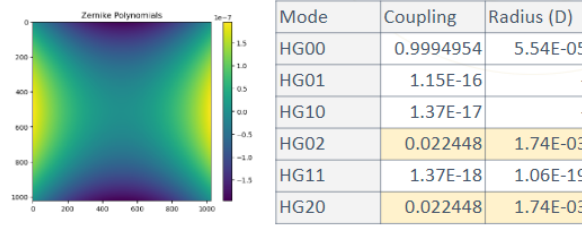


Figure 13: Vertical Astigmatic Mode Simulation

The vertical astigmatic mode shown above also most strongly couples to the HG_{02} and HG_{20} modes.

These simulations provide us with something to compare our actual results against, and allowed us to test our code pipeline to make sure it works.

4.2 Shack-Hartmann Wavefront Sensor Results

Using the microlens array shown in Fig. 6 and the setup we designed to us it in Fig. 9, we also imaged the mirror using the Shack-Hartmann Wavefront sensor. As we did with the Fizeau interferometer, we first imaged the flat mirror to gain a point of reference for taking data. This image is shown below, where Section 4.2 is the data directly from the CCD camera behind the microlens array, where the location of the dot's intensity relative to the center of each lens is an indication of a change in the wavefront. On the right, Section 4.2 is the reconstructed wavefront from this data.

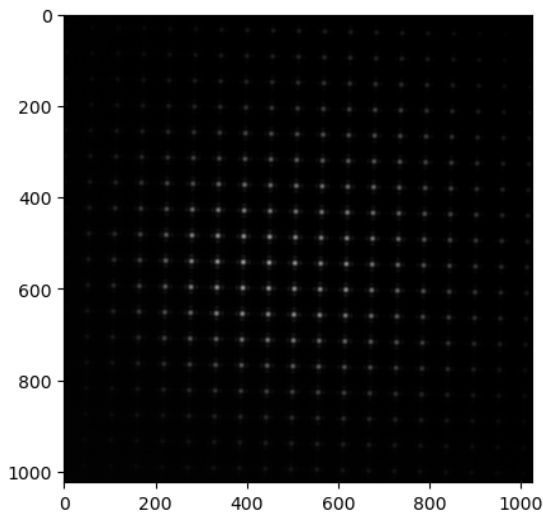


Figure 14: Flat mirror Shack-Hartmann Data

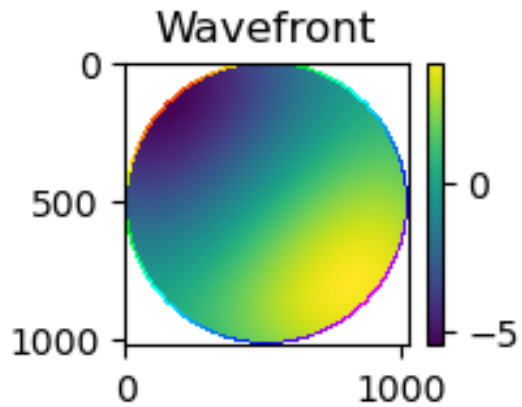


Figure 15: Flat mirror wavefront

While the data from Fig. 7 and Fig. 8 indicates that we should see an astigmatism, the wavefront that we see above is stronger than we should expect. We then applied a force to the mirror to lens the light into the oblique astigmatic mode (plus shape in Fig. 11). This is shown below in Section 4.2, the data from the Shack-Hartmann, and Section 4.2, the reconstructed wavefront.

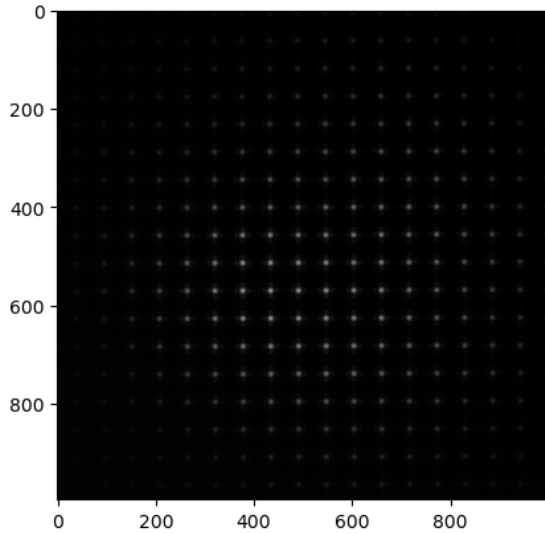


Figure 16: Oblique astigmatic Shack-Hartmann Data

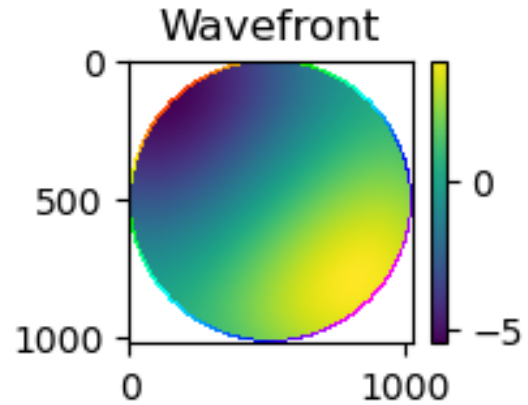


Figure 17: Oblique astigmatic wavefront

This wavefront looks incredibly similar to the previous, unstressed wavefront, even though the Zernike polynomials for each wavefront are different. In fact, if we subtract the two wavefronts, as we do in Fig. 18, we find that the two wavefronts are exactly the same. This indicates that the Shack-Hartmann Wavefront Sensor might not be precise enough to measure the changes in modes. This could also be a problem with our wavefront reconstruction, as the process uses an approximation to build the wavefront.

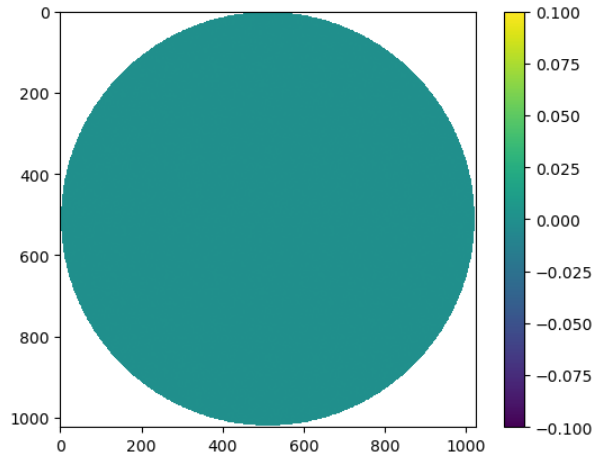


Figure 18: Flat wavefront subtracted from curved

One strategy we tried to rectify this was to zero out the contribution from the tip and the tilt of the mirror. Manually adjusting this had limited results, since all tip and tilt movements are coupled on the 5 axis stage, but simply ignoring the tilt components when reconstructing the wavefront showed some promise. We will be looking into this method further.

4.3 Fizeau interferometer results

Although we were not successful with the Shack-Hartmann Wavefront Sensor, we did use the Fizeau interferometer again to measure the wavefront, both with the mirror in the end mirror mount and with a mirror stressed into the different modes. Any stress of the mirror in the end mirror mount is caused by the half rings that hold it pressing on the mirror, so the mirror is not completely unstressed. The wavefront confirmed our earlier measurements that we took with the Fizeau interferometer.

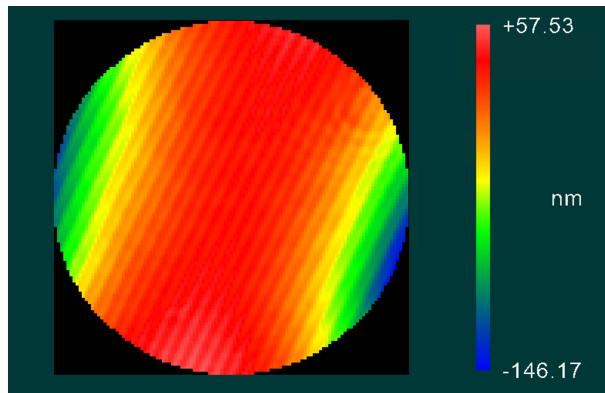


Figure 19: Unstressed wavefront

When the mirror was stressed into the oblique astigmatic mode, the original wavefront looks very similar to the unstressed case, as seen in Fig. 20. However, when we subtract out the wavefront of the mirror in the end mirror mount from the stressed one we get a wavefront that looks very similar to the characteristic 'plus' shape that we are looking for in Fig. 21. This subtraction is in effect removing the measurement from how the mirror was already curved and just showing us the change applied by the end mirror mount.

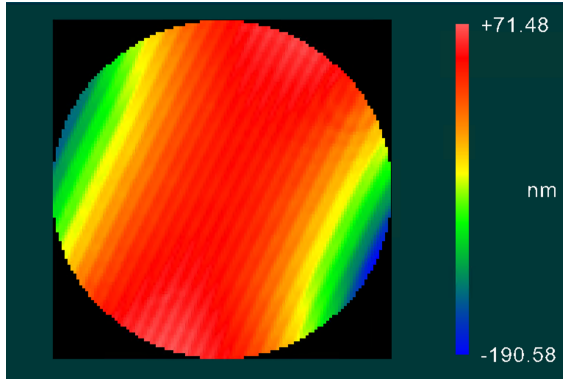


Figure 20: Oblique astigmatic mode

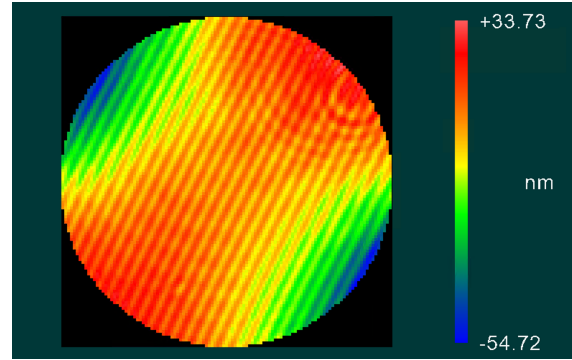


Figure 21: Oblique astigmatic mode minus unstressed wavefront

For the defocus mode, we completed the same process, however, we were not able to apply as much force to the mirror as we would have liked, without losing focus with the interferometer. In this case, we were not able to see the characteristic 'O' shape that we expected, instead when we see almost a flat surface in Fig. 23. This indicates that we did not successfully produce the defocus mode with the end mirror mount. This is expected by the simulation data, as the coupling coefficient to the modes is not as strong as it is for the astigmatic modes. This means that it would be more difficult to couple to this mode, which we found in our experiment.

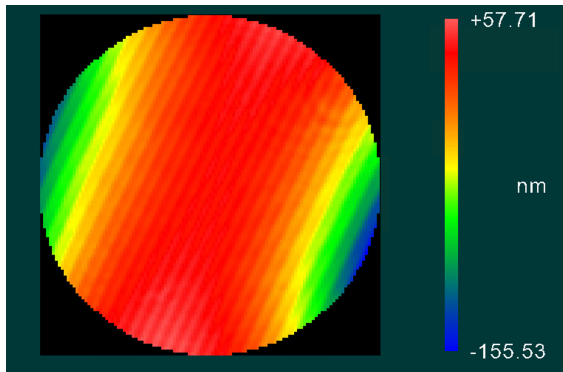


Figure 22: Defocus mode

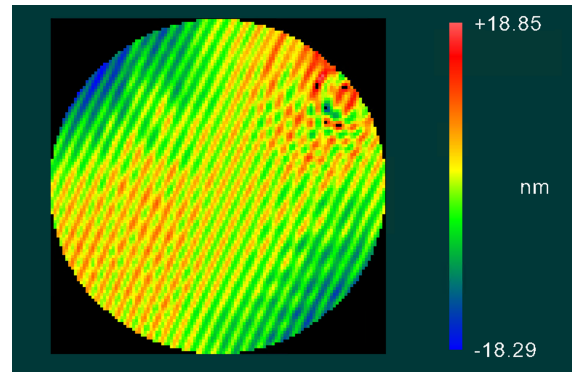


Figure 23: Defocus mode minus unstressed wavefront

We were able to strongly recreate the vertical astigmatic mode shown below in Fig. 24. Not only does it have the characteristic 'X' shape we are looking for, this shape looks even clearer when we subtract out the flat wavefront in Fig. 25. This wavefront measurement requires the most straightforward movement of the 'T' joints, as the vertical astigmatic mode only requires a bend in the spokes instead of twisting them.

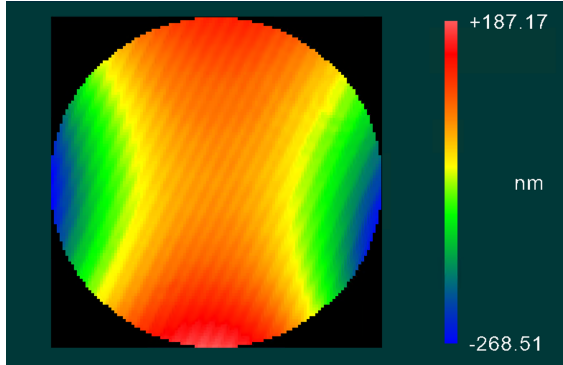


Figure 24: Vertical astigmatic mode

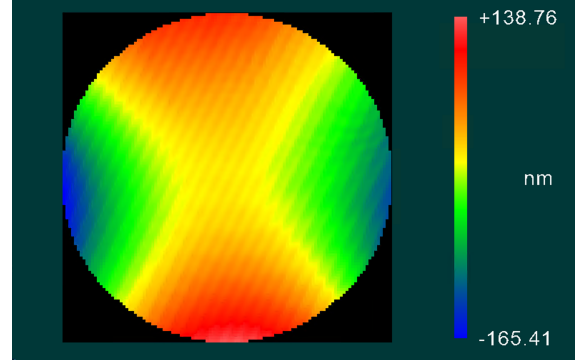


Figure 25: Vertical astigmatic mode minus unstressed wavefront

4.4 Coupling coefficient and radius of curvature

I used the wavefront data from the Fizeau interferometer to compute the coupling coefficient and radius of curvature, using the method we elaborated on before, and is done in Section 6. For all of the data, it is clear that we are most strongly coupled to the HG_{00} mode. This is what we expect, because we assume the entire incoming beam is in the HG_{00} mode, so we don't expect the light to coupling very strongly to a different mode because the wavelength of light is much larger than the curvature of the mirror.

The oblique astigmatic mode most strongly couples to the HG_{11} mode, as the coupling coefficient for that mode is larger than the corresponding coupling of the other modes. We see this in both the simulated oblique astigmatic mode and in the actual data from the Fizeau interferometer. Each of these modes corresponds to a radius that describes how much the mirror curves in this mode.

Plus Mode	Coefficient		Radius (D)	
	Simulated	Actual	Simulated	Actual
HG00	0.9994954	0.9999701	5.54E-05	3.27E-06
HG01	2.63E-17	1.20E-05	-	-
HG10	1.37E-17	1.02E-04	-	-
HG02	0.00071305	0.000123028	5.53E-05	1.59E-05
HG11	0.0317314	0.0010359	2.46E-03	8.03E-05
HG20	0.0007130	0.0002057	5.53E-05	9.54E-06

Figure 26: Oblique astigmatic mode coupling and radius

For the defocus mode, we would expect the actual data from the Fizeau interferometer to be most strongly coupled to the HG_{20} and HG_{02} mode. However, all of the observed coupling coefficients are around the same value, indicating that we did not strongly couple to any one mode. This is confirmed by looking at Fig. 23, which we see is flat mirror image.

o	Coefficient		Radius (D)	
mode	Simulated	Actual	Simulated	Actual
HG00	0.999999	0.999928	5.02E-14	7.85E-06
HG01	2.81E-17	7.83E-05	-	-
HG10	1.05E-17	3.28E-05	-	-
HG02	6.43E-07	5.36E-04	4.99E-08	3.07E-05
HG11	2.80E-18	1.42E-04	2.17E-19	1.10E-05
HG20	6.43E-07	3.96E-04	4.99E-08	4.15E-05

Figure 27: Defocus mode coupling and radius

For the vertical astigmatic mode, we had the closest match between the simulated and actual coupling. This, again, is confirmed visually by our data from the Fizeau interferometer, where the vertical astigmatic mode most closely matches the Z22 mode that we are trying to emulate. It is visible as well that our coupling coefficient is off by about an order of magnitude, which is something that we would like to investigate further.

x	Coefficient		Radius (D)	
mode	Simulated	Actual	Simulated	Actual
HG00	0.9994954	0.9999837	5.54E-05	1.78E-06
HG01	1.15E-16	7.60E-05	-	-
HG10	1.37E-17	6.20E-05	-	-
HG02	0.0224488	0.0021739	1.74E-03	2.23E-04
HG11	1.37E-18	3.44E-04	1.06E-19	2.67E-05
HG20	0.0224488	0.0028726	1.74E-03	1.69E-04

Figure 28: Vertical astigmatic mode coupling and radius

4.5 Computing Loss

As a measure of how well the wavefront matches the lower order modes is measuring the loss. We define loss as the amount of light that is lensed into modes higher than HG_{00} , HG_{10} , HG_{01} , HG_{20} , HG_{02} , and HG_{11} . This is light that we cannot control with our wavefront control methods, and therefore results in extra light in the interferometer, which we want to avoid. GQuEST has a loss budget of about 100 ppm (in terms of energy). Loss is calculated by finding the modulus squared of the coupling coefficient for the modes above and subtracting from one, which gives us the loss into higher order modes. This is given in Fig. 29.

	Simulated	Fizeau	Loss (ppm)
Flat mirror	8.66E-14	5.17E-05	51.7
Plus	1.02E-06	2.51E-05	25.1
O	8.82E-14	4.11E-05	41.1
X	1.02E-06	5.11E-05	51.1

Figure 29: Loss in each mode

The loss for each of these is lower than our noise budget for the mirror, which is promising. Also, the oblique astigmatic mode had the lowest loss, and therefore the most control of all the different modes we tried.

5 Conclusions and Next Steps

The goal of this project was to be able to map the GQuEST end mirrors for correcting the wavefront. We were successful in this goal, as the modes produced by the end mirror mount generally matches the COMSOL and python simulations. This is a positive first step towards making mirrors that match in modes with low loss.

We showed that we can properly lens into the astigmatic modes, but have difficulty doing so into the defocus mode. A next step will be to try to lens the wavefront into this mode again.

We also established that the Shack-Hartmann Sensor is not precise enough to measure changes in modes. The next steps for this project are to implement a different data analysis process for the Shack-Hartmann sensor to potentially improve its ability to reconstruct wavefronts. This could include using a zonal wavefront estimation method or some other algorithm in order to solve for the Zernike polynomials that allow us to recreate the wavefront.

Presently, we will continue to use and improve the pipeline for analyzing data, as well as seeing if we can optimize the way we solve for the coupling coefficient and radius. This will involve using new numerical methods to calculate the coupling for each of the different modes.

Another future goal will be to reduce the loss into higher order modes. This could be done by optimizing how much we turn the adjustment screws to lens into the mode. In the future, we will also be replacing these mirrors in the half ring with spokes and mirrors as one piece.

In addition, future designs will incorporate mirrors in which the spokes are a part of the mirror, as opposed to using a half ring that holds the silicon mirror. This upgrade will allow

the mirror to be deformed directly, instead of applying a force to the half ring. This can be seen in Fig. 30, and it will be incorporated in the next round of testing.

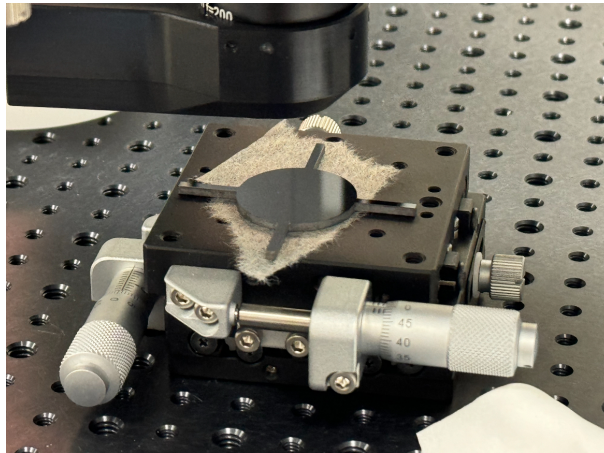


Figure 30: New mirror design

Another future step will of course be coating the mirrors with the high reflective and anti-reflective coating. More testing with the mirrors will need to be done once the mirrors are coated, with the specific goal of making the mirrors flat.

References

- ¹E. P. Verlinde and K. M. Zurek, “Observational signatures of quantum gravity in interferometers”, *Physics Letters B* **822**, 136663 (2021).
- ²S. M. Vermeulen, T. Cullen, D. Grass, I. A. O. MacMillan, A. J. Ramirez, J. Wack, B. Korzh, V. S. H. Lee, K. M. Zurek, C. Stoughton, and L. McCuller, *Photon counting interferometry to detect geotropic space-time fluctuations with gquest*, 2024.
- ³Wikipedia, *Gaussian beams*, 2024.
- ⁴*Zernike polynomials - Wikipedia — en.wikipedia.org*, https://en.wikipedia.org/wiki/Zernike_polynomials, [Accessed 01-08-2024].
- ⁵T. T. Kajava, H. M. Lauranto, and R. R. E. Salomaa, “Fizeau interferometer in spectral measurements”, *J. Opt. Soc. Am. B* **10**, 1980–1989 (1993).
- ⁶*Fused Silica Microlens Arrays — thorlabs.com*, https://www.thorlabs.com/newgrouppage9.cfm?objectgroup_id=2861&pn=MLA300-14AR, [Accessed 13-07-2024].
- ⁷R. Cubalchini, “Modal wave-front estimation from phase derivative measurements”, *J. Opt. Soc. Am.* **69**, 972–977 (1979).
- ⁸L. McCuller, “Ligo-t1900144-v3: beam layout requirements imposed by wavefront actuator”, LIGO Technical Note (2019).

Acknowledgements

This work was supported by the National Science Foundation Research Experience for Undergraduates (NSF REU) program, the LIGO Laboratory Summer Undergraduate Research Fellowship program (NSF LIGO), and the California Institute of Technology Student-Faculty Programs.

Huge thanks to GariLynn Billingsley for allowing us to use the Fizeau interferometer and for her help.

This work was also supported by mentors Daniel Grass and Prof. Lee McCuller and the entire GQuEST Lab at Caltech.

6 Appendix

6.1 Zernike Polynomials

We can define the Zernike polynomial in terms of the radial distance ρ , the azimuthal angle ϕ , the integer azimuthal degree m (where $m = 0$ for spherical polynomials, and n is the radial degree. These can be seen graphed in Fig. 4, from [4], where the radial degree increases moving down the pyramid and the corresponding azimuthal degree increases going across. The corresponding function is:

$$Z_n^m(\rho, \phi) = R_n^m(\rho) \cos(m\phi) \quad (6)$$

for even polynomials and is:

$$Z_n^{-m}(\rho, \phi) = R_n^m(\rho) \sin(m\phi) \quad (7)$$

for odd polynomials. The function $R_n^m(\rho)$ is known as the radial polynomial. It can be found by using the generating function:

$$R_n^m(\rho) = \sum_{k=0}^{\frac{n-m}{2}} \frac{(-1)^k (n-k)!}{k! \left(\frac{n+1}{2} - k\right)! \left(\frac{n-m}{2} - k\right)!} \rho^{n-2k} \quad (8)$$

functions that use integers to differentiate their modes is that we can combine the integers m and n to be known as another integer j , where:

$$j = \frac{n(n+1) + m}{2} \quad (9)$$

Using this fact, we can reconstruct the wavefront for some set amount of Zernike polynomials. This also allows us to understand the aberrations and deformations present in the optic under analysis, which can be seen in the final column below.

Z_n^m	Z_j	Classical name
Z_0^0	1	Piston
Z_1^{-1}	$2\rho \sin \phi$	Y-tilt
Z_1^1	$2\rho \cos \phi$	X-tilt
Z_2^{-2}	$\sqrt{6}\rho^2 \sin 2\phi$	oblique astigmatism
Z_2^0	$\sqrt{3}(2\rho^2 - 1)$	defocus
Z_2^2	$\sqrt{6}\rho^2 \cos 2\phi$	vertical astigmatism

6.2 Calculating the Coefficients of Zernike Polynomials from Radius

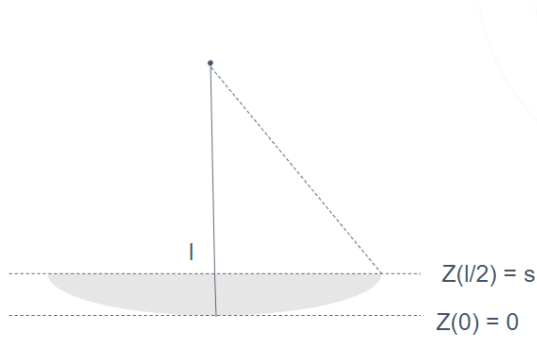


Figure 31: Initial conditions for Z values of mirror

Using the initial conditions of the location of the mirror, we can estimate what the coefficients a_{mn} of the Zernike Polynomials are in terms of the radius r , sagitta s , and the radius ρ . The wavefront $\Phi(x, y)$ is given by:

$$\Phi(\rho, \phi) = \sum a_{mn} Z_{mn}(\rho, \phi)$$

For the oblique astigmatic mode ($m = -2, n = 2$), we can say that:

$$Z_{-2,2}(\rho, \phi) = a_{-2,2}(\sqrt{6}\rho^2 \sin(2\phi))$$

And using the initial conditions above:

$$Z_{-2,2}(l/2, \pi/4) = a_{-2,2} \left(\sqrt{6} \left(\frac{l}{2} \right)^2 \sin\left(2 \cdot \frac{\pi}{4}\right) \right)$$

$$s = a_{-2,2} \left(\sqrt{6} \left(\frac{l^2}{2} \right) \sin\left(\frac{\pi}{2}\right) \right)$$

$$a_{-2,2} = \frac{s}{\sqrt{6}} \frac{4}{l^2}$$

Which gives us:

$$Z_{-2,2}(\rho, \phi) = \frac{4s}{l^2} (\rho^2 \sin(2\phi))$$

Which is what was used in our simulation in Fig. 11. This formula also holds for $Z(0, \phi) = 0$ for any ϕ .

For the defocus mode, which is $m = 2, n = 0$ we can do much the same:

$$Z_{2,0}(\rho, \phi) = a_{2,0}(2\rho^2 - 1)$$

$$Z_{2,0}(l/2, \pi/4) = a_{2,0} \left(2 \left(\frac{l}{2} \right)^2 - 1 \right)$$

$$s = a_{2,0} \left(\left(\frac{l^2}{2} \right) - 1 \right)$$

$$a_{2,0} = \frac{s}{\left(\frac{l^2}{2} \right) - 1}$$

Which gives us:

$$Z_{2,0}(\rho, \phi) = \frac{s}{\left(\frac{l^2}{2} \right) - 1} (2\rho^2 - 1)$$

Which was again used in our simulation. Finally for the vertical astigmatic mode $m = n = 2$, we get:

$$Z_{2,2}(\rho, \phi) = a_{2,2}(\sqrt{6}\rho^2 \cos(2\phi))$$

And using the initial conditions above:

$$Z_{2,2}(l/2, 0) = a_{2,2} \left(\sqrt{6} \left(\frac{l}{2} \right)^2 \cos(2 \cdot 0) \right)$$

$$s = a_{2,2} \left(\sqrt{6} \left(\frac{l^2}{2} \right) \right)$$

$$a_{2,2} = \frac{s}{\sqrt{6}} \frac{4}{l^2}$$

Which gives us:

$$Z_{2,2}(\rho, \phi) = \frac{4s}{\sqrt{6} l^2} (\rho^2 \cos(2\phi))$$

6.3 Zernike Vandermonde Matrix

Analyzing the the Shack-Hartman data requires us to use the properties of Zernike polynomials to create a least squares equation that we can solve. This process is outlined by [7], which establishes a way to analyze wavefronts from phase derivative measurements like Hartman sensors, that measure local changes in the mirror distortion. We can say that the estimate of the wavefront $\Phi(x, y)$ is given by:

$$\Phi(x, y) = \sum_{i=1}^I a_i Z_i(x, y) \quad (10)$$

Where a is a Zernike coefficient and $Z_i(x, y)$ is the Zernike polynomial for a total of i polynomials that we are fitting. We exclude $i = 0$, since it is constant. Since we only have derivative measurements of the wavefront phase, our estimate looks more like:

$$\frac{\partial \Phi}{\partial x} = \sum_{i=1}^I a_i \frac{\partial Z_i(x, y)}{\partial x} \quad (11)$$

in the x direction and

$$\frac{\partial \Phi}{\partial y} = \sum_{i=1}^I a_i \frac{\partial Z_i(x, y)}{\partial y} \quad (12)$$

in the y direction. This process relies on matrices, and we create a Vandermonde matrix of the derivatives of zernike polynomials and a matrix of the derivative of the location of the beam placement. The first vector is P , which represents the values of the local shifts in x and y for a total number of microlenses k :

$$P = (\text{x shift 1, x shift 2, } \dots \text{ x shift } k, \text{ y shift 1, y shift 2} \dots \text{y shift } k)^t \quad (13)$$

This can be thought of as the 'shifts' of each of the microlenses. It is the directional derivative of the phase, at a particular location in the microlens.

Since our P vector is the directional derivative, we need to take the derivatives of the Zernike polynomials as well in order to solve the least squares estimation and find the coefficients in Eq. (10). We can setup a matrix of our derivatives of the polynomials as:

$$D = \begin{pmatrix} \frac{\partial Z_2(x,y)_1}{\partial x} & \frac{\partial Z_2(x,y)_2}{\partial x} & \dots & \frac{\partial Z_2(x,y)_1}{\partial y} & \dots & \frac{\partial Z_2(x,y)_k}{\partial y} \\ \dots & \dots & \dots & \dots & \dots & \dots \\ \frac{\partial Z_i(x,y)_1}{\partial x} & \frac{\partial Z_i(x,y)_2}{\partial x} & \dots & \frac{\partial Z_i(x,y)_1}{\partial y} & \dots & \frac{\partial Z_i(x,y)_k}{\partial y} \end{pmatrix} \quad (14)$$

Where k is the same in both matrices, meaning we can multiply P and D . The matrix we are solving for is our coefficients, A :

$$A = (a_1, a_2, a_3 \dots a_i) \quad (15)$$

Once we have these coefficients, we can use Eq. (10) to solve for the wavefront. Using these matrices together, we can solve the least squares expression.

$$\begin{aligned} P &= D^t A \\ DP &= DD^t A \\ A &= (DD^t)^{-1} DP \end{aligned}$$

Where t refers to the transpose of the matrix and -1 is the inverse. So the coefficients a_i that we need to solve for are determined by the directional derivatives of the Zernike polynomials at each of the sampling locations of the microlens.

6.4 Determining the radius of curvature from coupling coefficient

As mentioned in Section 1, we are able to use Eq. (2) to determine the radius of curvature of the mirror. This process in one dimension is elaborated on in [8], but here we use two.

The equation for a Gaussian beam in two dimensions is:

$$\begin{aligned} u_{nm}(x, y) &= \left(\frac{1}{2^{n+m-1} n! m! \pi} \right)^{1/2} \left(\frac{1}{w_0} \right) \left(\frac{q_0}{q(z)} \right) \left(\frac{q_0 q^*(z)}{q_0^* q(z)} \right)^{n+m/2} \\ &\quad H_n \left(\frac{\sqrt{2}x}{w(z)} \right) H_m \left(\frac{\sqrt{2}y}{w(z)} \right) \exp \left(-ik \frac{(x^2 + y^2)}{2R} \right) \exp \left(-\frac{(x^2 + y^2)}{w^2} \right) \end{aligned} \quad (16)$$

The equation for the beam in the HG_{00} mode is:

$$u_{00}(x, y) = \left(\frac{2}{\pi} \right)^{1/2} \left(\frac{1}{w_0} \right) H_0 \left(\frac{\sqrt{2}x}{w(z)} \right) H_0 \left(\frac{\sqrt{2}y}{w(z)} \right) \exp \left(-ik \frac{(x^2 + y^2)}{2R} \right) \exp \left(-\frac{(x^2 + y^2)}{w^2} \right) \quad (17)$$

where we normalize to remove the Gouy phase terms. This is similar for the HG_{02} mode:

$$u_{02}(x, y) = \left(\frac{1}{4\pi} \right)^{1/2} \left(\frac{1}{w_0} \right) H_0 \left(\frac{\sqrt{2}x}{w(z)} \right) H_2 \left(\frac{\sqrt{2}y}{w(z)} \right) \exp \left(-ik \frac{(x^2 + y^2)}{2R} \right) \exp \left(-\frac{(x^2 + y^2)}{w^2} \right) \quad (18)$$

$$k_{0000}(x, y) = \left(\frac{2}{\pi} \right) \left(\frac{1}{w_0^2} \right) \int \int e^{ikDx^2/2} e^{-2x^2/w^2} e^{-2y^2/w^2} dx dy \quad (19)$$

and likewise for the HG_{02} mode:

$$k_{0002}(x, y) = \left(\frac{1}{2} \right)^{1/2} \left(\frac{1}{w_0^2 \pi} \right) \int \int H_2 \left(\frac{\sqrt{2}y}{w(z)} \right) e^{ikDx^2/2} e^{-2x^2/w^2} e^{-2y^2/w^2} dx dy \quad (20)$$

We can make substitutions that will reduce some of the constants we have, namely that:

$$x' = \frac{\sqrt{2}x}{w}$$

and that

$$y' = \frac{\sqrt{2}y}{w}$$

Which gives us that:

$$k_{0000}(x', y') = \frac{1}{\pi} \int \int \exp \left[\frac{ikDw^2x'^2}{4} \right] e^{-x'^2} e^{-y'^2} dx' dy' \quad (21)$$

for the HG_{00} to HG_{00} mode, and that:

$$k_{0002}(x', y') = \frac{1}{\sqrt{8\pi}} \int \int H_2(y') \exp \left[\frac{ikDw^2x'^2}{4} \right] e^{-x'^2} e^{-y'^2} dx' dy' \quad (22)$$

for the HG_{00} to HG_{02} mode.

Using Gaussian integrals and Hermite polynomials we can solve the above equations.

$$H_2(x) = 4x^2 - 2 \quad (23)$$

and

$$\int_{-\infty}^{\infty} e^{-\alpha x^2} x^{2n} dx = \sqrt{\frac{\pi}{\alpha}} \frac{(2n-1)!!}{2\alpha^n} \quad (24)$$

And let us also make the substitution:

$$a = \frac{kDw^2}{4}$$

$$\alpha = 1 - ia$$

Where α can be plugged in to the formula above.

Which gives us:

$$k_{0000}(x', y') = \sqrt{\frac{\frac{kDw^2}{4}}{(1 - i\frac{kDw^2}{4})^{3/2}}} \quad (25)$$

$$k_{0002}(x', y') = \frac{1}{\sqrt{2}} \frac{\frac{kDw^2}{4}}{(1 - i\frac{kDw^2}{4})^{3/2}} \quad (26)$$